

🔗 Refraction and Straining of Near-Inertial Waves by Barotropic Eddies

OLIVIER ASSELIN

Scripps Institution of Oceanography, University of California, San Diego, La Jolla, California

LEIF N. THOMAS

Department of Earth System Science, Stanford University, Stanford, California

WILLIAM R. YOUNG

Scripps Institution of Oceanography, University of California, San Diego, La Jolla, California

LUC RAINVILLE

Applied Physics Laboratory, University of Washington, Seattle, Washington

(Manuscript received 19 May 2020, in final form 31 July 2020)

ABSTRACT: Fast-moving synoptic-scale atmospheric disturbances produce large-scale near-inertial waves in the ocean mixed layer. In this paper, we analyze the distortion of such waves by smaller-scale barotropic eddies, with a focus on the evolution of the horizontal wavevector \mathbf{k} under the effects of straining and refraction. The model is initialized with a horizontally uniform ($\mathbf{k} = 0$) surface-confined near-inertial wave, which then evolves according to the phase-averaged model of Young and Ben Jelloul. A steady barotropic vortex dipole is first considered. Shear bands appear in the jet region as wave energy propagates downward and toward the anticyclone. When measured at a fixed location, both horizontal and vertical wavenumbers grow linearly with the time t elapsed since generation such that their ratio, the slope of wave bands, is time independent. Analogy with passive scalar dynamics suggests that straining should result in the exponential growth of $|\mathbf{k}|$. Here instead, straining is ineffective, not only at the jet center, but also in its confluent and diffluent regions. Low modes rapidly escape below the anticyclonic core such that weakly dispersive high modes dominate in the surface layer. In the weakly dispersive limit, $\mathbf{k} = -t\nabla\zeta(x, y, t)/2$ provided that (i) the eddy vertical vorticity ζ evolves according to the barotropic quasigeostrophic equation and (ii) $\mathbf{k} = 0$ initially. In steady flows, straining is ineffective because \mathbf{k} is always perpendicular to the flow. In unsteady flows, straining modifies the vorticity gradient and hence \mathbf{k} , and may account for significant wave–eddy energy transfers.

KEYWORDS: Anticyclones; Internal waves; Mesoscale processes

1. Introduction

Atmospheric storms sweeping across the ocean resonantly excite near-inertial waves, or internal waves oscillating at a frequency close to f , the Coriolis frequency (Alford et al. 2016). These waves originate within a shallow surface mixed layer, but with the large horizontal scale characteristic of synoptic weather systems (Pollard 1980; Thomson and Huggett 1981). Given such anisotropic primordial scales, wind-generated near-inertial waves are inefficient at radiating their energy into the ocean interior (Gill 1984). A reduction in the horizontal length scale of the wave is necessary to increase the vertical group velocity and enable propagation into the ocean interior.

Three contender scale-reduction mechanisms are summarized on the right-hand side of the ray-tracing formula for the evolution of the horizontal wavenumber $\mathbf{k} = (k, l)$:

$$\frac{d_g}{dt} \begin{pmatrix} k \\ l \end{pmatrix} = \underbrace{-\beta \begin{pmatrix} 0 \\ 1 \end{pmatrix}}_{\beta\text{-refraction}} - \underbrace{\frac{1}{2} \begin{pmatrix} \zeta_x \\ \zeta_y \end{pmatrix}}_{\zeta\text{-refraction}} - \underbrace{\begin{pmatrix} U_x & V_x \\ U_y & V_y \end{pmatrix} \begin{pmatrix} k \\ l \end{pmatrix}}_{\text{straining}}, \quad (1)$$

where d_g/dt is a derivative following the group velocity. The three processes on the right-hand side— β -refraction, ζ -refraction, and straining—tend to increase $|\mathbf{k}|$, i.e., decrease the horizontal length scale of a freshly generated near-inertial wave.

The Ocean Storms Experiment (D'Asaro 1989; D'Asaro et al. 1995) provided observational evidence that the latitudinal variation in the Coriolis frequency, $\beta = df/dy$, leads to a linear growth of the meridional wavenumber l . In (1), this corresponds to a dominant balance in which β -refraction is the main term on the right, implying $l = l_0 - \beta t$. In physical terms, the southernmost and northernmost portions of the primordial wave experience slightly different inertial frequencies. Over time, this frequency shift results in phase decoherence in the meridional direction, which is equivalent to an increase of l .

🔗 Denotes content that is immediately available upon publication as open access.

📎 Supplemental information related to this paper is available at the Journals Online website: <https://doi.org/10.1175/JPO-D-20-0109.s1>.

Corresponding author: Olivier Asselin, oasselin@ucsd.edu

DOI: 10.1175/JPO-D-20-0109.1

© 2020 American Meteorological Society. For information regarding reuse of this content and general copyright information, consult the [AMS Copyright Policy](#) (www.ametsoc.org/PUBSReuseLicenses).

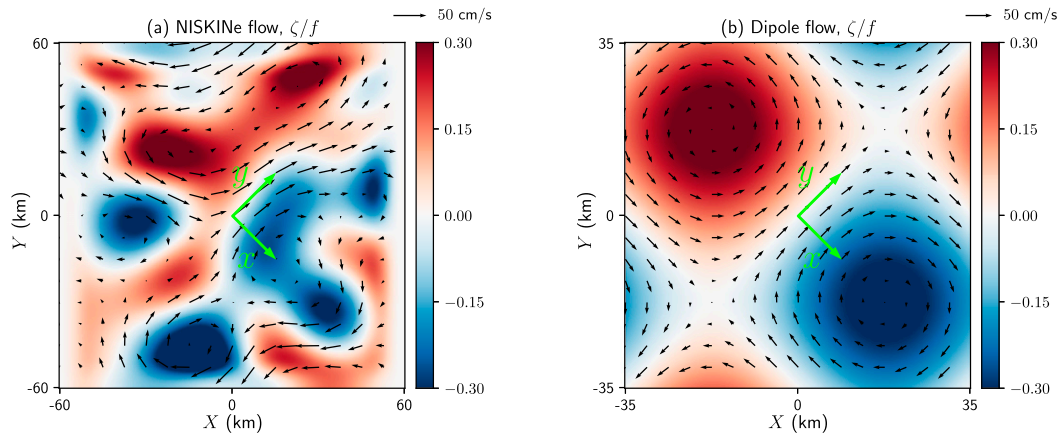


FIG. 1. Normalized vertical relative vorticity map from (a) NISKINE and (b) its idealized, dipole version. The rotated axes, (x, y) , used for analysis are shown in green. The relation between the two coordinate sets is $(X, Y) = (x + y, y - x)/\sqrt{2}$.

Gradients in the vertical vorticity, $\zeta = V_x - U_y$, with (U, V) the horizontal velocity of mesoscale eddies, can also reduce the initial horizontal wave scale (Kunze 1985; Young and Ben Jelloul 1997). Near-inertial waves embedded in a field of eddies experience different rotation rates in cyclonic and anticyclonic regions, such that the wave phase acquires the 10–100-km scale of eddies. This process is ζ -refraction in (1). For spatially uniform and steady vorticity gradients, ζ -refraction also produces a linear growth of the wavevector, $\mathbf{k} = \mathbf{k}_0 - (1/2)t\nabla\zeta$. Because mesoscale eddies typically have $|\nabla\zeta| \gg \beta$, one expects that ζ -refraction is more rapid than β -refraction (Van Meurs 1998). For this reason we shall assume constant planetary vorticity f and neglect β -refraction throughout this paper.

Differential advection by mesoscale eddies stretches and rotates the wavevector \mathbf{k} . This process is captured by the straining term in (1). By analogy with passive-scalar advection, one expects straining to cause an exponential growth of $|\mathbf{k}|$ (Jones 1969). In strain-dominated regions, and with sufficient vertical shear, the horizontal and vertical wavenumbers both grow exponentially so that the group velocity goes to zero. Provided uniform velocity gradients along a ray, waves are captured and strained into oblivion (Bühler and McIntyre 2005). Polzin (2008) argues that the vertical profiles of horizontal velocity observed during the Mid-Ocean Dynamics Experiment are consistent with wave capture by mesoscale straining.

What are the respective roles of straining and ζ -refraction in shaping \mathbf{k} in a generic geostrophic flow in which the two processes are at play? Naively, one would expect strong-enough straining to dominate ζ -refraction because straining produces exponential-in-time growth of $|\mathbf{k}|$, while refraction results only in linear-in-time growth. We show here, however, that this expectation may be violated in the important case of a wind-generated near-inertial wave, for which the initial horizontal scale is large, provided that the background flow is barotropic.

This insight emerged from the Near-Inertial Shear and Kinetic Energy experiment (NISKINE), a research initiative

funded by the U.S. Office of Naval Research with a field work component focused in a region located about 500 km south of Iceland. In a companion paper, Thomas et al. (2020) provide observational evidence of the ζ -refraction of a wind-generated near-inertial wave in a barotropic vortex dipole. A few inertial periods after the wind event, the phase differences in the inertial velocities are consistent with a linear growth of \mathbf{k} at a rate comparable to half the local vorticity gradient. This is despite the fact that ballpark estimates indicate that straining is strong enough to produce an exponential growth of $|\mathbf{k}|$. Why does straining appear to be ineffective in the NISKINE dipole? Furthermore, mesoscale vorticity in the NISKINE region undergoes significant changes over a few inertial periods. How do these rapid changes in mesoscale vorticity variations affect ζ -refraction and straining?

2. Problem formulation

a. Flow setup

Figure 1a shows an estimate of the horizontally non-divergent flow observed during the NISKINE cruise based on satellite altimetry refined by in situ velocity measurements from both ship-mounted and drifting instruments (Thomas et al. 2020). Vertical profiles reveal a surprisingly uniform flow vertical structure in the top several hundred meters of the ocean, motivating the assumption of barotropic flow throughout this paper. Analysis of wave evolution in this complex flow field is confined to section 6 of this paper. In the next few sections, we limit attention to an idealized, dipole model of the NISKINE flow shown in Fig. 1b.

The dipole is best defined using a coordinate system that is rotated by 45° relative to the cardinal directions, represented by the (X, Y) axes in Fig. 1. This rotated (x, y) coordinate system is shown by the green axes in Fig. 1. The x axis is antiparallel to the vorticity gradient at the origin. In terms of the rotated coordinates the dipole streamfunction is

$$\psi = U\kappa^{-1} \sin\kappa x \cos\kappa y. \quad (2)$$

The vorticity is $\zeta = -2\kappa^2\psi$, or

$$\zeta = -\gamma\kappa^{-1} \sin\kappa x \cos\kappa y, \quad (3)$$

where $\gamma \stackrel{\text{def}}{=} 2\kappa^2 U$. The scales of the dipole flow are set to fit both the observed velocity maximum at the center of the NISKINe jet, $U = 33.5 \text{ cm s}^{-1}$, and the observed maximum vorticity gradient, $\gamma = 2.7 \times 10^{-9} \text{ m}^{-1} \text{ s}^{-1}$. This requires $\kappa = \sqrt{2\pi}/(70 \text{ km})$. The resulting root-mean-square Rossby number is $\kappa U/f \approx 0.17$, with a maximum of 0.34. Despite these numbers not being reassuringly small, the flow is assumed to obey quasigeostrophic dynamics, whose validity has been shown to extend to Rossby numbers of order 0.1 (e.g., Klein et al. 2008; Asselin et al. 2018).

NISKINe is near 58.5°N , so $\beta \sim 10^{-11} \text{ m}^{-1} \text{ s}^{-1}$ is two orders of magnitude smaller than the maximum relative vorticity gradient, γ . We thus neglect the latitudinal dependence of the Coriolis frequency and set $f = 1.24 \times 10^{-4} \text{ s}^{-1}$. In the (X, Y) coordinate system used for the axes in Fig. 1, the domain is horizontally periodic with equal east–west (X) and north–south (Y) dimensions of 70 km. The depth is $H = 3 \text{ km}$. Stratification is vertically uniform. Unless otherwise specified, the square of the buoyancy frequency used in the calculations is $N^2 = 10^{-5} \text{ s}^{-2}$.

b. Waves

Our idealized scenario consists of a fast-moving, large-scale atmospheric disturbance impulsively exciting horizontally uniform near-inertial oscillations in the mixed layer. Following Gill (1984), we focus on the wake stage where wind stress is no longer acting. Crucially, we assume that the initial inertial currents have scales much larger than the $O(50) \text{ km}$ scale of eddies. As such, our model is inappropriate for small-scale or slow-moving atmospheric disturbances (Geisler 1970; Price 1983; D’Asaro 1985; Nilsson 1995). These ideal conditions are met by the fast-moving storm that generated the near-inertial wave reported by Thomas et al. (2020).

Mathematically, our scenario translates into an initial value problem for the waves, with a near-inertial oscillation initially confined to a surface layer,

$$u(t = 0) = u_0 \exp(-z^2/\sigma^2), \quad v(t = 0) = 0. \quad (4)$$

The inertial oscillations begin with an eastward velocity $u_0 = 10 \text{ cm s}^{-1}$ over a surface layer of depth $\sigma = 30 \text{ m}$. Since stratification is depth independent in our model, σ does not represent a mixed layer depth. Instead, we refer to σ as the surface layer depth, i.e., the depth over which momentum is initially injected by winds.

It is insightful to express wave variables in terms of the back rotated velocity,

$$LA = (u + iv)e^{ift}, \quad (5)$$

where $A(x, y, z, t)$ is a space- and time-dependent complex field and

$$L = \frac{\partial}{\partial z} \left(\frac{f^2}{N^2} \frac{\partial}{\partial z} \right) \quad (6)$$

is a frequently occurring operator. Thus, LA is the slowly evolving envelope of the near-inertial wave, and its leading-order evolution is dictated by the Young–Ben Jelloul (YBJ) equation (Young and Ben Jelloul 1997),

$$\partial_t LA + J(\psi, LA) + i \left(\beta y + \frac{\zeta}{2} \right) LA + \frac{if}{2} \Delta A = 0, \quad (7)$$

where $J(a, b) \stackrel{\text{def}}{=} a_x b_y - a_y b_x$ is the Jacobian and $\Delta \stackrel{\text{def}}{=} \partial_x^2 + \partial_y^2$ is the horizontal Laplacian. From left to right, the YBJ equation expresses the changes to the near-inertial wave envelope due to advection by the mean flow, refraction by planetary and relative vorticity, and dispersion.

c. Numerics

Although the analysis is carried out in the classic YBJ framework, numerical integrations are performed using the YBJ⁺ equation (Asselin and Young 2019). This equation is identical to (7), except that the operator L is replaced with

$$L^+ \stackrel{\text{def}}{=} L + \frac{1}{4} \Delta. \quad (8)$$

This tweak in the definition of the wave envelope brings the twin advantages of higher accuracy and lower computational effort while maintaining ease of implementation (Asselin and Young 2019).

The YBJ⁺ model is pseudospectral in the x and y directions, allowing horizontal derivatives to be computed with spectral accuracy. The 2/3 rule is used to remove aliased modes (Durrán 2013). Vertical derivatives are approximated with second-order centered finite differences. Time integration is accomplished with the leapfrog scheme with weak time diffusion (Asselin 1972). Weak horizontal hyperdiffusion is applied to filter out subgrid horizontal wave scales.

3. The dipole solution

We begin by presenting the general appearance of the full YBJ solution (7) for a large-scale near-inertial wave (4) evolving in the steady dipole flow (Fig. 1b). The dipole solution shows strong accumulation of wave energy in the anticyclonic core of the dipole with little energy left in the cyclonic core after a few inertial periods (Fig. 2, top panels). This rapid attraction of wave energy by anticyclones has been observed repeatedly (Weller 1985; Kunze 1986; Kunze et al. 1995; Elipot et al. 2010; Jaimes and Shay 2010). Explanations have been proposed that rely on the broadening of the allowable frequency band in negative vorticity regions (Kunze 1985), appeals to the quantum analogy between energy wells and negative vorticity (Balmforth et al. 1998; Rocha et al. 2018), and a conservation law for steady barotropic flows (Danioux et al. 2015).

Vertical sections (middle panels of Fig. 2) reveal that wave energy is drained down the anticyclonic pipe (Lee and Niiler 1998; Asselin and Young 2020). In the process, wave shear bands form symmetrically about the anticyclonic axis (bottom panels of Fig. 2), with phase contours propagating upward and

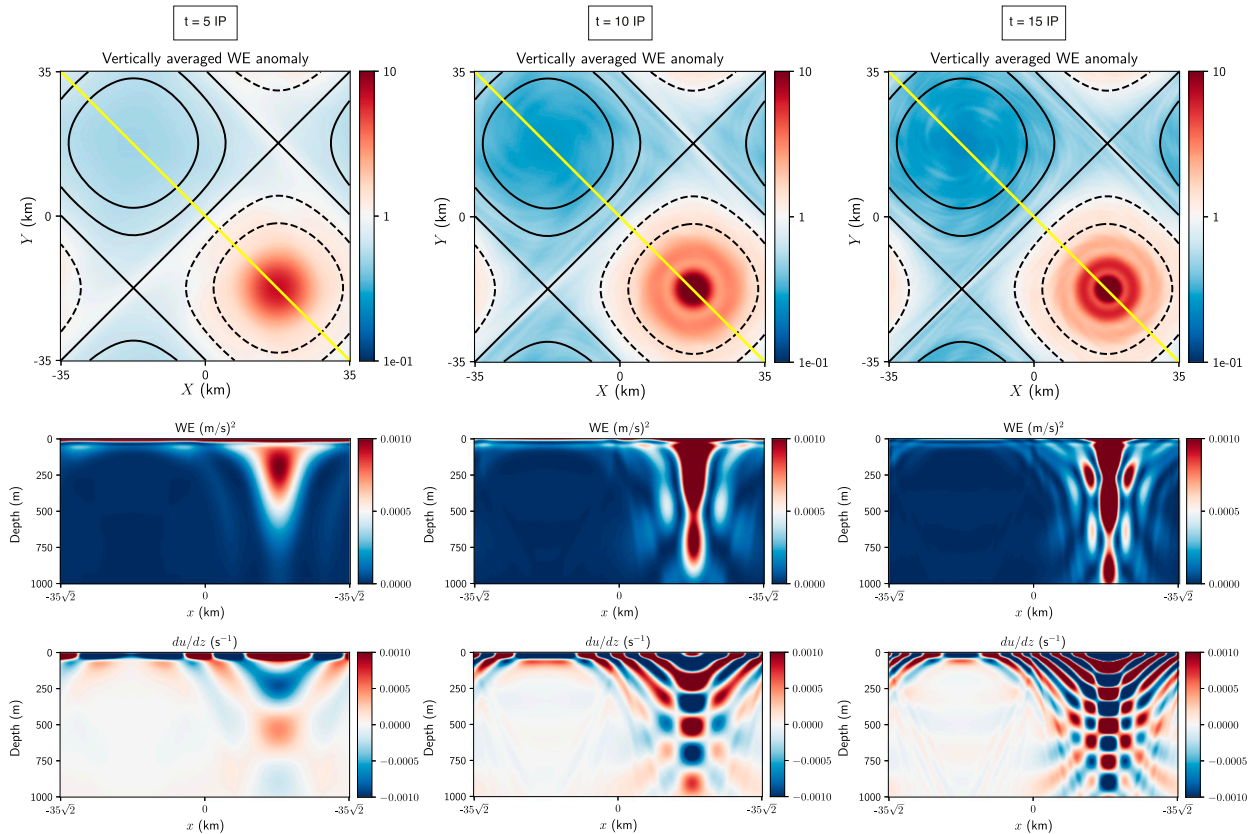


FIG. 2. Dipole solution with $N^2 = 10^{-5} \text{ s}^{-2}$. (top) Vertically averaged wave energy (WE) anomaly on a logarithmic scale. Vorticity contours of 0, $\pm 0.1f$ and $\pm 0.2f$ are overlaid. (middle) Vertical cuts of WE along the yellow line drawn in top panels ($y = 0$). (bottom) Vertical cuts of eastward wave velocity shear, also along the yellow transect. Time increases from left to right: 5, 10, and 15 inertial periods.

toward the anticyclone center (see the online supplemental material for an animated version of the plot). The shear bands have a clear, dominant wavelength that shrinks with time. The slope of the bands steepens slightly with depth, but remains independent of time. In agreement with WKB scaling, the slope of the shear bands becomes gentler as stratification is increased (Fig. 3). That is, the vertical wavenumber increases with N while the horizontal wavenumber seems largely unaffected.

What explains the shape of the bands, with a single dominant wavelength at any given time, nearly straight but steepening

slope with increasing depth and decreasing stratification, and why is their slope time independent? These questions are the focus of the next section.

4. Refraction

As a starting point, we consider the wave evolution in the presence of ζ -refraction alone, i.e., neglecting straining in (1). While this premise is strictly valid only near the jet center, its implications turn out to be insightful and apply over a broader region than anticipated. We begin by using a heuristic approach to understand the shear bands properties reported in

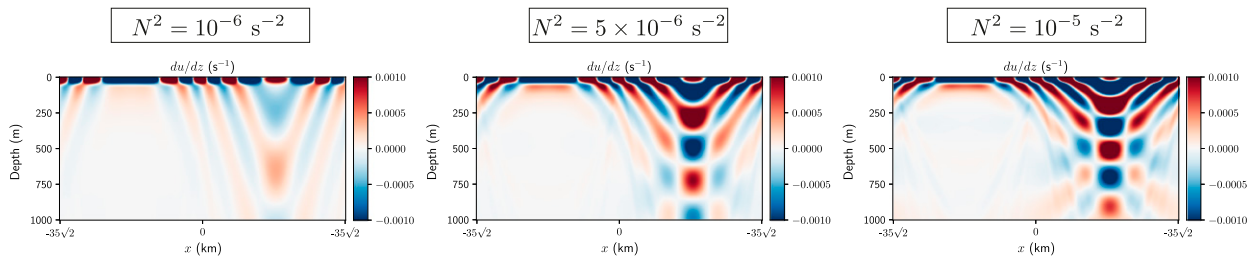


FIG. 3. Wave shear bands in the dipole solution. Each panel shows a different value of stratification, increasing from left to right. The vertical slices are along the yellow line drawn in top panels of Fig. 2 ($y = 0$). Snapshots are shown after 10 inertial periods.

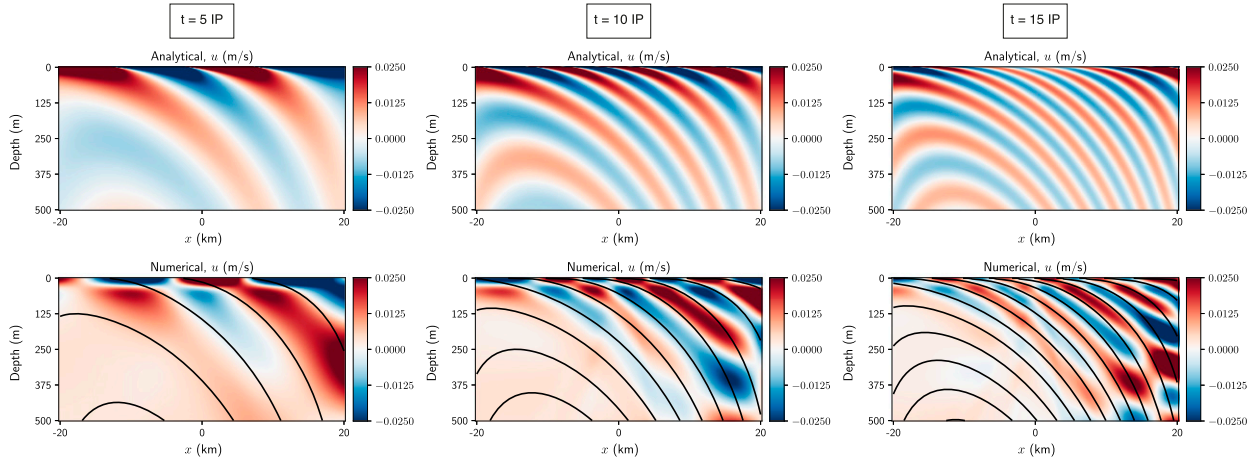


FIG. 4. Vertical cuts of the zonal wave velocity u after 5, 10, and 15 inertial periods along $y = 0$. (top) Leading-order analytical solution, (A19), using the x -dependent $\nabla\zeta$. (bottom) Solution of the full numerical model with overlaid $u = 0$ contours from the analytical solution.

section 3. These heuristic results are confirmed in appendix A, where a derivation of the linear wave solution is presented for an arbitrary steady vorticity gradient profile with weak spatial variability.

a. Wavevector evolution at the jet center

Let us consider the wavevector evolution near the center of the dipole jet. For simplicity, we assume a uniform vorticity gradient, $\nabla\zeta = -\gamma\hat{x}$ with $\gamma > 0$. At $t = 0$, near-inertial oscillations are horizontally uniform and confined to the ocean surface layer (4). Then, ζ -refraction causes an initial linear growth of the wavevector along the vorticity gradient,

$$k = \frac{1}{2}\gamma t, \quad l = 0. \tag{9}$$

Although we are considering the center of the jet, where velocity is maximum, $\mathbf{U} = (0, U)$, the wavevector (9) is perpendicular to the flow and the Doppler shift, $\mathbf{U} \cdot \mathbf{k}$, is zero. This justifies the neglect of advection throughout this section. In

section 6, the neglect of advection is shown to be less restrictive than one might suppose.

The inertial wave is initially confined to a shallow surface layer, and thus projects on a broad spectrum of vertical wavenumbers m . This compact initial disturbance then disperses as a wave train. Because the flow is barotropic and N is constant, m is constant along a ray. And because there is no Doppler shifting, wave energy propagates at the intrinsic group velocity,

$$c_g^x = \frac{N^2}{fm^2} \frac{\gamma t}{2}, \quad c_g^y = 0, \quad c_g^z = -\frac{N^2}{fm^3} \left(\frac{\gamma t}{2}\right)^2, \tag{10}$$

where $\gamma t/2$ is the horizontal wavenumber in (9). Wave energy propagates downward at vertical group velocity $c_g^z \sim m^{-3}$ so there is a dominant vertical wavelength at a given depth and time. To quantify this, we integrate c_g^z with respect to time:

$$z(t) = \int_0^t c_g^z(t') dt' = -\frac{N^2 \gamma^2}{12 f m^3} t^3, \tag{11}$$

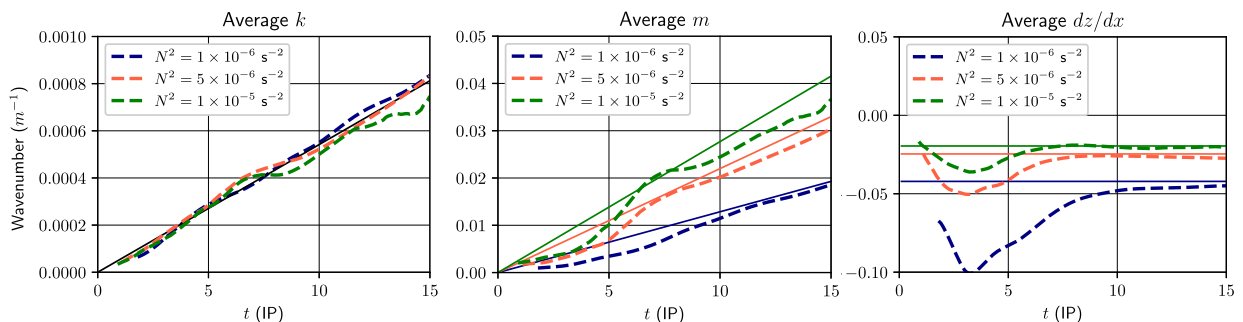


FIG. 5. (left) Horizontal wavenumber, (center) vertical wavenumber, and (right) slope of the wave bands from the numerical YBJ solution (dotted; see appendix B), spatially averaged over the jet center region, $x \in [5, 15]$ km, $y = 0$, and $z \in [-100, 300]$ m. Different colors indicate different stratifications. To reduce noise only regions with wave energy above $10^{-5} \text{ m}^2 \text{ s}^{-2}$ are included in the average. For comparison, predictions (A23), (A24), and (13) are shown (solid lines).

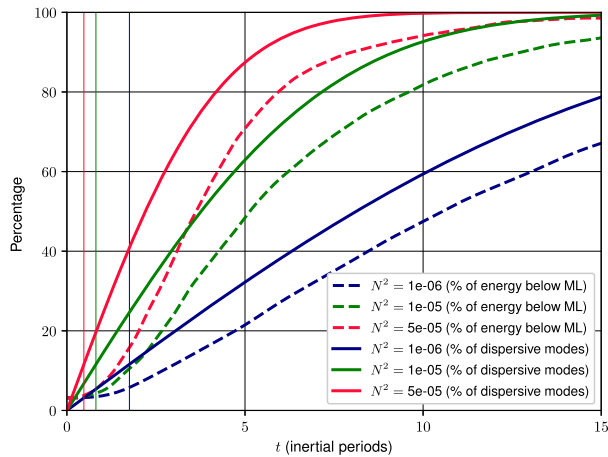


FIG. 6. Fraction of energy in wavenumbers $m < m_c(t)$ estimated from the heuristic solution (solid curves) vs the fraction of wave energy below the surface layer from the numerical solution (dashed curves). Vertical lines correspond to t_H in (22).

where we have applied the initial condition $z(0) = 0$. Inverting the above expression for m , one finds

$$m = \left(\frac{N^2 \gamma^2}{12f|z|} \right)^{1/3} t, \tag{12}$$

where $|z|$ is the (positive) depth.

At fixed depth z , both k and m grow linearly with time (9)–(12), consistent with Fig. 2. Furthermore, the wave band slope, defined as

$$\frac{dz}{dx} = \frac{k}{m} = - \left(\frac{3f\gamma|z|}{2N^2} \right)^{1/3}, \tag{13}$$

is time independent (Fig. 2). The band slope increases proportionally to $|z|^{1/3}$, consistent with the weak steepening of

bands with depth (Fig. 2). Finally, (13) goes like $N^{-2/3}$ such that higher stratification is associated with gentler band slopes (Fig. 3).

b. Validation of heuristic arguments using analytical and numerical solutions

Analytical and numerical solutions to the YBJ equation are used to test these predictions from the heuristic arguments. The analytical solution is obtained from linearizing the YBJ equation and is described in appendix A [see Eq. (A19)]. This analytical solution generalizes the heuristic predictions to encompass arbitrary, but slowly varying vorticity gradients $\nabla\zeta$. Near the jet center, where $\nabla\zeta \approx -\gamma\hat{x}$, the generalized predictions for the horizontal and vertical wavenumbers, (A23) and (A24), reduce to the heuristic predictions, (9) and (12). As a bonus, the analytical derivation predicts not only the wavevector, but also the wave amplitude.

The analytical solution is compared to the numerical solution of the full YBJ equation in Fig. 4. Near the surface and in the jet region, the analytical solution captures the salient features of the shear bands—the shrinking of their dominant wavelength, the steepening of their slope with depth and their time-invariant shape. The cyclone-anticyclone energy gradient, however, is not captured due to the assumption of slowly varying vorticity gradient. The analytical solution also fails near the core of the anticyclone because rays emitted from the other side of the anticyclone interfere with the locally emitted rays (see Fig. 3).

The wavevector predicted by (A23) and (A24) agrees quantitatively with the full YBJ solution (Fig. 5). Both k and m increase linearly at the predicted rate. Stratification leaves k essentially unchanged, while the growth rate of m increases with stratification. In turn, shear bands are steeper in regions of weak stratification (Fig. 3). Since both k and m increase linearly with time, the wave band slope asymptotes to a constant value (13).

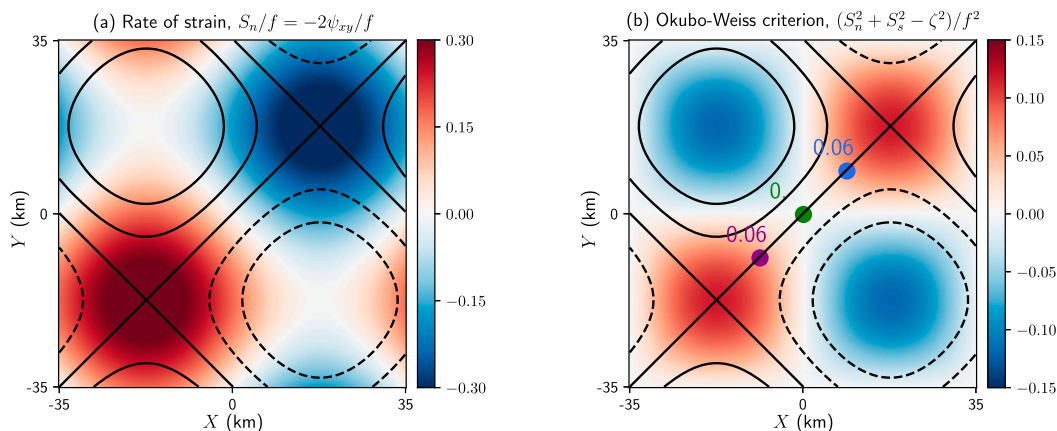


FIG. 7. (a) Normalized rate of strain (note that the other component, S_s , is zero for the dipole) and (b) Okubo-Weiss criterion, which identifies straining- (>0) vs vorticity-dominated (<0) regions of the domain. Local values of the Okubo-Weiss criterion are indicated in the confluent (purple), jet (green), and diffluent (blue) regions. Vorticity contours of $0, \pm 0.1f$, and $\pm 0.2f$ are overlaid.

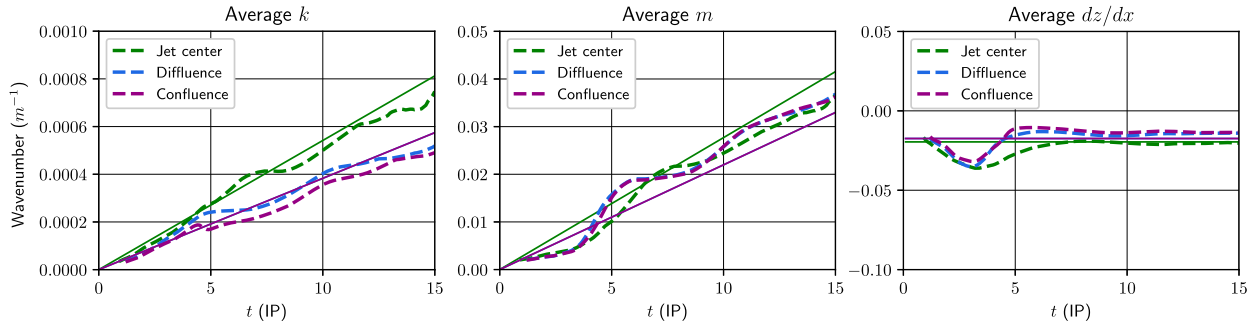


FIG. 8. (left) Horizontal wavenumber, (center) vertical wavenumber, and (right) slope of the wave bands from the numerical YBJ solution (dotted; see appendix B), spatially averaged over $x \in [5, 15]$ km, $z \in [-100, 300]$ m. Colors specify the location on the y axis, i.e., the confluent ($\kappa y = -\pi/4$, purple), jet center ($y = 0$; green), and diffluent ($\kappa y = +\pi/4$, blue) regions shown as dots in Fig. 7b. Superimposed in solid lines are the ζ -refraction predictions, (A23), (A24), and (13), based on the local vorticity gradient. The solid purple line depicts the identical predictions for the confluence and diffluence regions. To reduce noise only regions with wave energy above $10^{-5} \text{ (m s}^{-1}\text{)}^2$ are included in the average.

c. Backtracking wave bands

Conservation of Eulerian wave frequency ω in a steady flow allows one to backtrack the surface origin of wave bands observed at depth. The full dispersion relation of the f -plane YBJ equation (7) is

$$\omega = \mathbf{U} \cdot \mathbf{k} + \frac{f}{2}(\text{Ro} + \text{Bu}), \tag{14}$$

where ω is the wave frequency in excess of f , and the vorticity-based Rossby number and wave Burger number are

$$\text{Ro} \stackrel{\text{def}}{=} \frac{\zeta}{f}, \quad \text{Bu} \stackrel{\text{def}}{=} \left(\frac{N|\mathbf{k}|}{fm} \right)^2. \tag{15}$$

As we have seen, the Doppler shift is negligible near the jet center such that the intrinsic frequency,

$$\omega_i = \frac{f}{2}(\text{Ro} + \text{Bu}), \tag{16}$$

is also conserved in its vicinity. Therefore, the sum of Bu and Ro remains constant as the wave propagates. One can thus backtrack wind-generated wave bands observed at depth in steady barotropic eddies. If wave bands are observed in a region with $\text{Ro}^* = \zeta^*/f$ with scales corresponding to Bu^* , then the wave must have originated from a surface region where $\text{Ro} = \text{Ro}^* + \text{Bu}^*$.

d. Damping of sea surface near-inertial oscillations

The heuristic solution provides a time scale for the radiative damping of sea surface near-inertial oscillations. The time taken for a disturbance with a wavenumber m to propagate to a depth z is obtained by rearranging (12)

$$t = \left(\frac{12f|z|}{N^2\gamma^2} \right)^{1/3} m. \tag{17}$$

After a given time t , all disturbances with wavenumbers from $m = 0$ up to $m(z, t)$ in (12) have reached a depth z or below. To obtain a rough time estimate of wave energy radiation below the mixed layer, a cutoff $m_c(t)$ is defined by replacing z with the surface layer depth σ in (12)

$$m_c(t) = \left(\frac{N^2\gamma^2}{12f\sigma} \right)^{1/3} t. \tag{18}$$

In a barotropic flow, the vertical wavenumber spectrum of wave energy is time independent, and thus can be obtained from a Fourier transform of the wave initial condition (4)

$$\mathcal{E}(m) = \frac{1}{2} |\widehat{\text{LA}}_0(m)|^2 \propto \exp(-m^2\sigma^2/2). \tag{19}$$

One estimates the fraction of wave energy radiated out of the surface layer by integrating $\mathcal{E}(m)$ from $m = 0$ to $m_c(t)$:

$$\frac{\text{WE}_{\text{rad}}(t)}{\text{WE}_{\text{tot}}} \approx \frac{\int_0^{m_c(t)} \mathcal{E}(m) dm}{\int_0^\infty \mathcal{E}(m) dm} = \text{erf} \left[\frac{m_c(t)\sigma}{\sqrt{2}} \right], \tag{20}$$

where erf denotes the error function.

In Fig. 6, we compare (20) (dashed lines) with the fraction of energy below the surface layer in the full numerical solution (solid lines). The heuristic solution (20) overestimates the rapidity of downward radiation. A rationalization of this discrepancy is that the heuristic calculation uses the maximum vorticity gradient γ in (18) and thus overestimates the cutoff wavenumber $m_c(t)$. The heuristic estimate also assumes that once a disturbance reaches the surface layer base, its energy is fully located below the surface layer.

To compress the information in (20) we define a characteristic time scale t_σ by equating the argument of erf in (20) to one; $\text{erf}(1) = 0.84$, meaning that 16% of the initial energy is left in the surface layer at $t = t_\sigma$. Thus, we obtain the radiative damping time scale

$$t_\sigma = \left(\frac{2^{3/2}12f}{N^2\gamma^2\sigma^2} \right)^{1/3}. \tag{21}$$

Moehlis and Llewellyn Smith (2001, hereafter MLS) considered the radiative damping of a mixed layer induced by β -refraction. The MLS model has a weakly stratified mixed layer of depth H_{mix} sitting above a uniformly stratified interior ocean. (We use uniform N over the whole depth H and so do

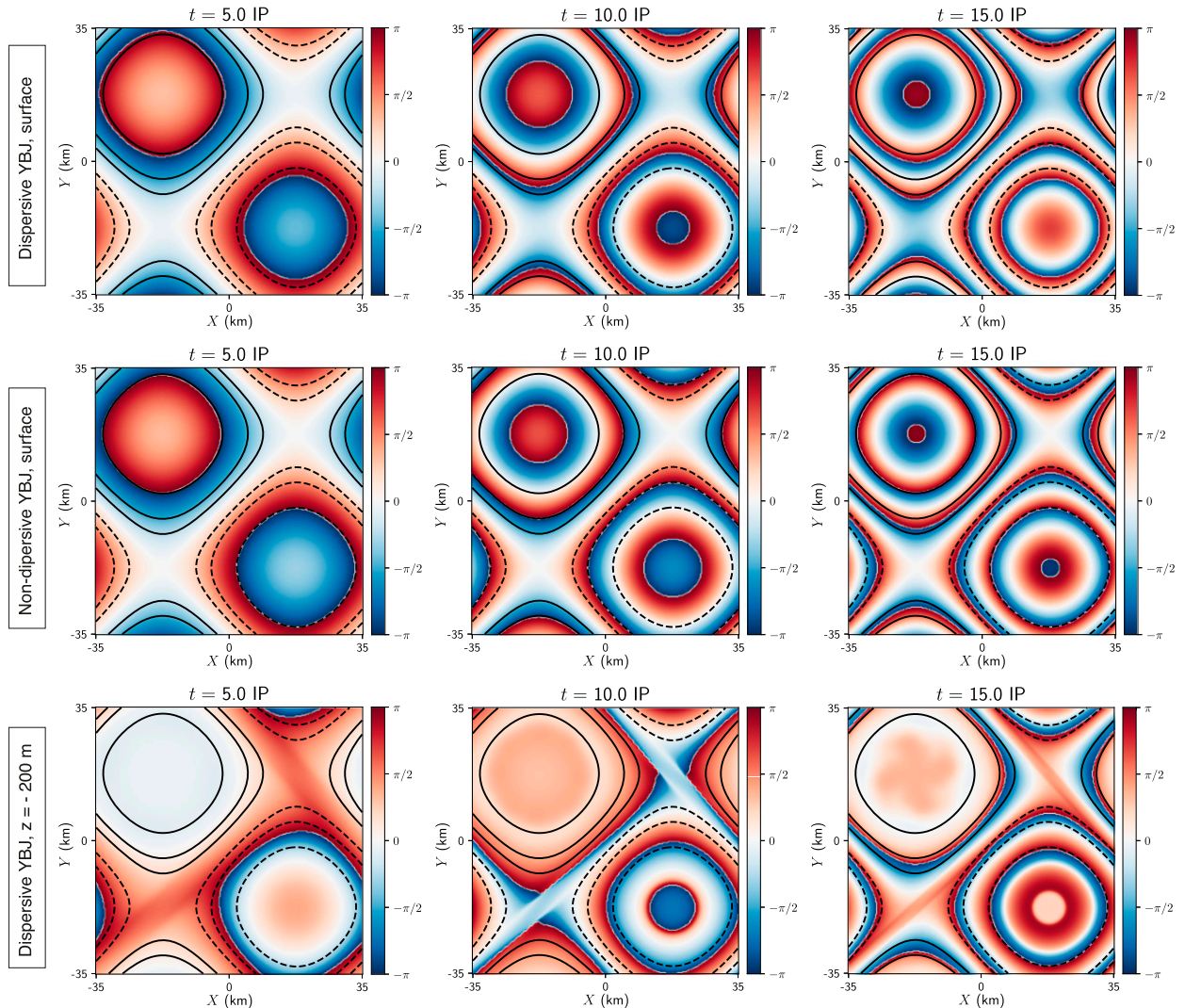


FIG. 9. Evolution of the wave phase $[\theta = \tan^{-1}(v/u)$; colors] in the dipole flow. (top) Sea surface θ for the from the full, dispersive YBJ system, (7), with $N^2 = 10^{-5} \text{ s}^{-2}$. (middle) Sea surface θ for the nondispersive YBJ solution, (7) with the ΔA term set to zero. (bottom) θ at a depth of 200 m in the full, dispersive YBJ system, (7), with $N^2 = 10^{-5} \text{ s}^{-2}$. Contours are for vorticity values of 0, ± 0.05 , $\pm 0.1f$, and $\pm 0.2f$.

not explicitly model the mixed layer.) Despite the mixed layer model, and aside from numerical factors of order unity, the time scale identified by MLS is the same as (21) with γ replaced by β and σ replaced by H_{mix} . In particular, the radiative damping time scale is independent of the mixed layer stratification (if any).

How does the radiative-damping time scale (21) compare with previous estimates of the mixed layer decay time scale? Gill (1984) proposed that the decay scale can be estimated as the time needed for the gravest vertical mode to undergo a phase change of 90° . D’Asaro (1989) adapted this idea to estimate the decay scale due to β -refraction. For a constant- N flow with a background vorticity gradient $|\gamma| \gg \beta$, this estimate is

$$t_H = \left(\frac{12\pi^3 f}{N^2 \gamma^2 H^2} \right)^{1/3}, \tag{22}$$

where the H subscript emphasizes that t_H depends on the full ocean depth H . Aside from numerical constants, t_σ is larger than t_H by the factor $(H/\sigma)^{2/3} \gg 1$. Indeed, t_H badly underestimates the time needed for a significant loss of the surface-layer energy: see the vertical colored lines in Fig. 6.

5. Straining

Thus far we have considered wave evolution close to the jet center. In this special location, the rate of strain vanishes, i.e., $\psi_{xy} = \psi_{xx} - \psi_{yy} = 0$ (Fig. 7a). The Doppler shift, $\mathbf{U} \cdot \mathbf{k}$, is also zero because \mathbf{k} is antiparallel to $\nabla\zeta$, so perpendicular to \mathbf{U} . What about straining-dominated regions, such as the dipole’s confluent and diffluent regions? How does straining affect the wavevector \mathbf{k} ?

Bühler and McIntyre (2005) examined straining by a steady uniform shear (thus eliminating ζ -refraction, which relies on second-order spatial derivatives of velocity). In this case, analytical solutions can be found for the evolution of the

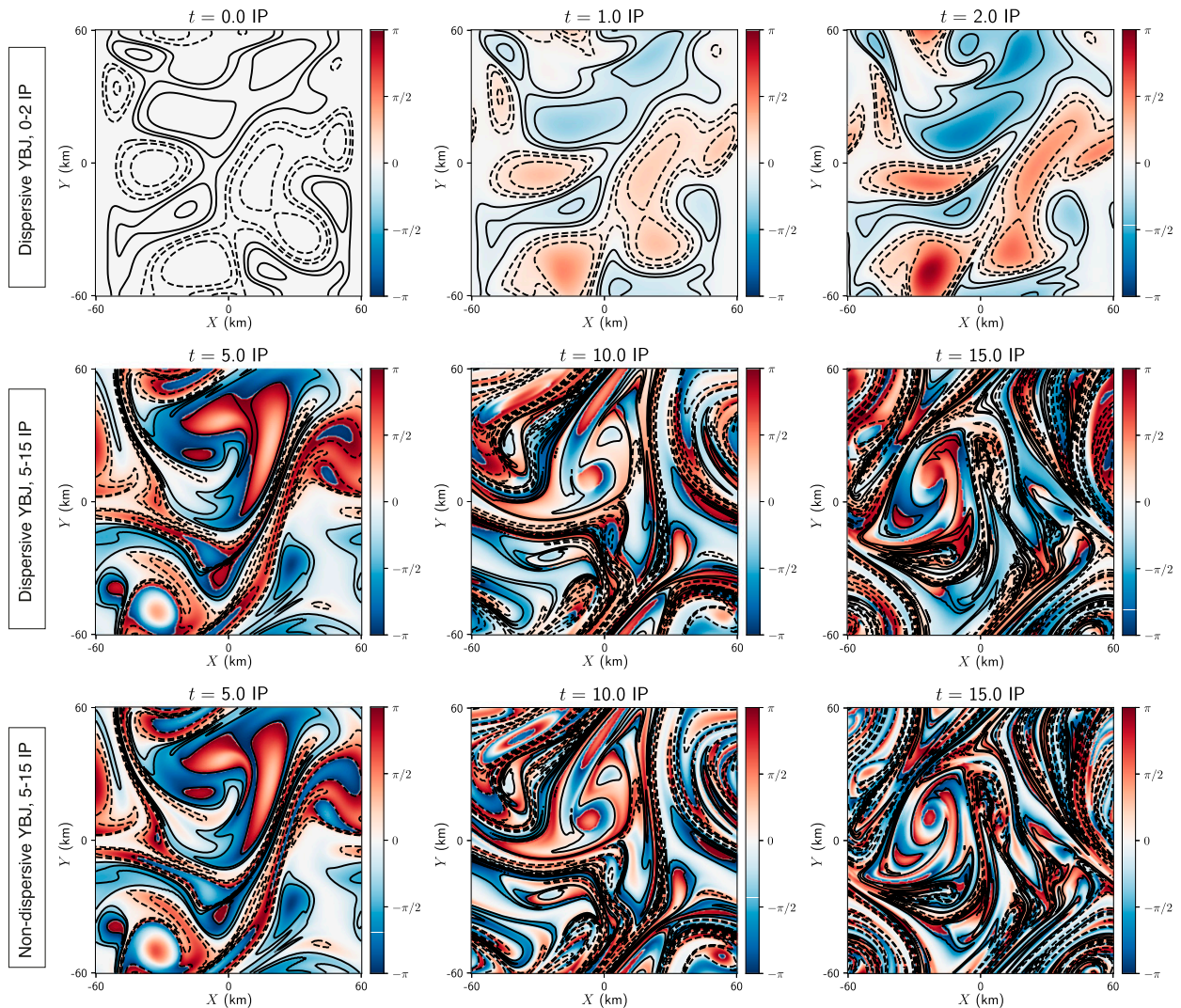


FIG. 10. Evolution of the sea surface wave phase $[\theta = \tan^{-1}(v/u)$; colors]. The top and middle panels show the solution of the full, dispersive YBJ system, (7), with $N^2 = 10^{-5} \text{ s}^{-2}$ coupled with a flow evolving according to the barotropic quasigeostrophic equation, (34). The NISKIne flow (Fig. 1a) is used as an initial condition. Contours are for vorticity values of 0, $\pm 0.05f$, $\pm 0.1f$, and $\pm 0.2f$. For comparison, the bottom panels show the solution of the nondispersive YBJ system for the same times as the middle panels: 5, 10, and 15 inertial periods.

packet-following three-dimensional wavevector (Jones 1969). In a barotropic flow, the rate-of-strain tensor in (1) can be separated into two distinct contributions:

$$\begin{pmatrix} U_x & V_x \\ U_y & V_y \end{pmatrix} = \frac{1}{2} \begin{pmatrix} S_n & S_s \\ S_s & -S_n \end{pmatrix} + \frac{1}{2} \begin{pmatrix} 0 & \zeta \\ -\zeta & 0 \end{pmatrix}, \quad (23)$$

where $S_n \stackrel{\text{def}}{=} U_x - V_y = -2\psi_{xy}$ and $S_s \stackrel{\text{def}}{=} U_y + V_x = \psi_{xx} - \psi_{yy}$ are the normal and shear components of the rate-of-strain tensor, respectively. The first term of (23) tends to increase $|\mathbf{k}|$ exponentially in time; the second term, on its own, rotates \mathbf{k} with a frequency $\zeta/2$. In regions of positive Okubo–Weiss criterion (shown for the dipole in Fig. 7b),

$$OW = S_n^2 + S_s^2 - \zeta^2, \quad (24)$$

the wavevector \mathbf{k} should undergo exponential growth with an e -folding time scale $OW^{-1/2}$ (Bühler and McIntyre 2005). Is this the case in the dipole solution?

Although the confluent and diffluent regions are characterized by $OW/f^2 = \pm 0.06$, corresponding to an e -folding time scale of $OW^{-1/2} \approx 0.7$ inertial period, there is no sign of a wavevector exponential growth, even after 15 inertial periods (Fig. 8). In fact, the refraction-only predictions (A23) and (A24) are as good at capturing k and m in the confluent and diffluent regions as they are in the jet center (Fig. 5). In other words, ζ -refraction alone accounts for the wavevector evolution, and straining is ineffective. Why is that?

A first clue comes from the work of Rocha et al. (2018). In a barotropic flow, vertical modes are uncoupled. For any given vertical mode, the horizontal group velocity,

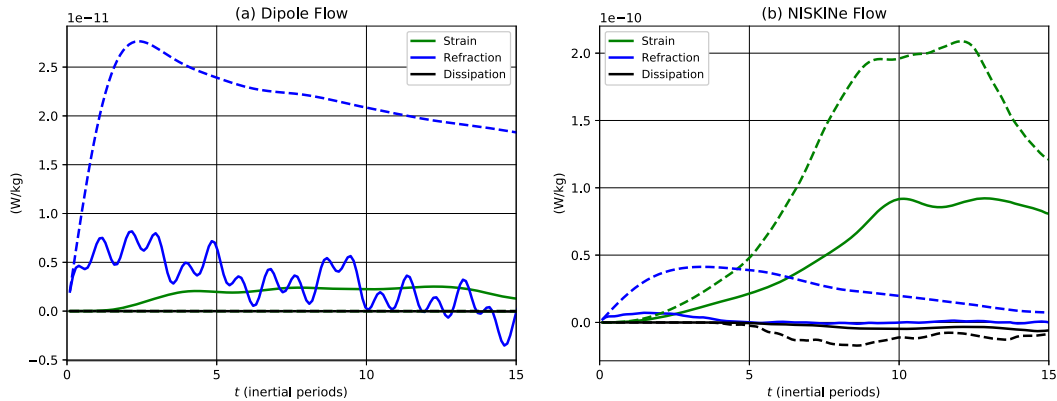


FIG. 11. Wave potential energy production via refraction (45) and straining (46), and loss via dissipation, for (a) the dipole and (b) NISKINe flows, with (solid) and without (dashed) dissipation.

$$\mathbf{c}_g^h = \hbar \mathbf{k}, \tag{25}$$

where $\hbar = N^2/fm^2$ is the wave dispersivity, grows linearly with \mathbf{k} . As straining exponentially compresses wave crests, the horizontal group velocity also increases exponentially. Thus, if \hbar is large enough, the wave rapidly escapes the straining region and its growth is no longer exponential. This is consistent with low- m disturbances leaving the jet region to accumulate in the anticyclone.

But what about weakly dispersive waves, for which \hbar is small and escape is slow? Why do not we observe exponential growth for the weakly dispersive modes left in the jet region? To answer these questions, we now consider the combined effects of refraction and straining in the limit of weak dispersion.

6. Weak dispersion

The two previous sections considered refraction and straining separately, focusing on the case of the dipole flow. Along the jet’s confluent, diffluent, and center regions, $\mathbf{k} \approx -t\nabla\zeta/2$. This is consistent with ζ -refraction, but inconsistent with straining. In this section, we consider the evolution of \mathbf{k} under the combined effects of refraction and straining, but also \mathbf{k} -advection, $J(\psi, \mathbf{k})$, which has so far received limited attention. The limit of weak dispersion proves enlightening not only to explain why straining is ineffective in the dipole, but also yields a remarkably simple analytical wave solution for arbitrary barotropic flows.

a. General wavevector evolution

Let us first consider general near-inertial wave dynamics for an arbitrary barotropic flow. We begin by decomposing the wave field into vertical normal modes:

$$LA(x, y, z, t) = -\sum_{n=1}^{\infty} r_n^{-2} A_n(x, y, t) g_n(z), \tag{26}$$

where g_n is the vertical eigenmode and r_n the Rossby radius of the n th vertical mode. Substituting (26) into the YBJ equation (7) yields decoupled equations for each vertical mode:

$$\partial_t A_n + J(\psi, A_n) + i\left(\beta y + \frac{\zeta}{2}\right) A_n - \frac{i}{2} \hbar_n \Delta A_n = 0, \tag{27}$$

where $\hbar_n \equiv r_n^2/f$ is the dispersivity of mode n . Following Klein et al. (2004) we write the wave envelope as $A_n = R_n e^{i\theta_n}$, where R_n and θ_n are the real-valued amplitude and phase. Substituting into (27) and separating the real and imaginary parts:

$$\partial_t R + J(\psi, R) = -\frac{\hbar}{2} (2\nabla R \cdot \nabla \theta + \Delta \theta R), \tag{28}$$

$$\partial_t \theta + J(\psi, \theta) = -\left(\beta y + \frac{\zeta}{2}\right) + \frac{\hbar}{2} \left(\frac{\Delta R}{R} - |\mathbf{k}|^2\right), \tag{29}$$

where we have lightened the notation by dropping the mode index n . The above equations are an exact reformulation of the YBJ equation for an arbitrary barotropic flow and arbitrary stratification. Note that (29) is a generalized version of the dispersion relation (14), where $\theta_t \equiv -\omega$ and $J(\psi, \theta)$ is the Doppler shift.

The evolution of the wavevector is obtained by taking the horizontal gradient of (29):

$$\begin{aligned} \partial_t \mathbf{k} + \underbrace{J(\psi, \mathbf{k})}_{\mathbf{k}\text{-advection}} + \underbrace{J(\nabla\psi, \theta)}_{\text{straining}} &= \underbrace{-\beta \hat{y}}_{\beta\text{-refraction}} \underbrace{-\frac{1}{2} \nabla \zeta}_{\zeta\text{-refraction}} \\ &+ \underbrace{\frac{\hbar}{2} \nabla \left(\frac{\Delta R}{R}\right) - (\mathbf{c}_g^h \cdot \nabla) \mathbf{k}}_{\text{dispersive effects}}. \end{aligned} \tag{30}$$

Equation (30) incorporates all processes discussed so far— β -refraction, ζ -refraction, and straining—but also group velocity propagation and \mathbf{k} -advection, which appear in the ray derivative on the left-hand side of (1):

$$\frac{d_g \mathbf{k}}{dt} \stackrel{\text{def}}{=} \partial_t \mathbf{k} + J(\psi, \mathbf{k}) + (\mathbf{c}_g^h \cdot \nabla) \mathbf{k}. \tag{31}$$

The ray tracing formula (1) is the WKB approximation of (30), and differs from it only by neglecting the dispersive term $\hbar \nabla(\Delta R/2R)$. Otherwise, (30) amounts to the geometrical optics equation of Lighthill (1978) and Kunze et al. (1995) written in an Eulerian frame. This simple reframing, however, turns out

to be insightful because the usual wave-following ray-tracing Eq. (1) conceals a near-cancellation between \mathbf{k} -advection and straining for large-scale inertial waves in steady barotropic eddies. To see this, we consider the limit of weak dispersion, $\hbar \rightarrow 0$.

b. Weakly dispersive limit: An analytical solution

In the weakly dispersive wave limit, $\hbar \rightarrow 0$, only the local, instantaneous vorticity gradient affects the wavevector of an initially uniform inertial wave. Crucially, this holds true not only for the dipole case, but for *any* barotropic quasigeostrophic flow, steady or unsteady. When $\hbar \rightarrow 0$, the phase–amplitude formulation of the f -plane YBJ in (28) and (29), simplifies to

$$\partial_t R + J(\psi, R) = 0, \tag{32}$$

$$\partial_t \theta + J(\psi, \theta) = -\frac{1}{2}\zeta. \tag{33}$$

The equations above are solved alongside the barotropic quasigeostrophic equation:

$$\partial_t \zeta + J(\psi, \zeta) = 0. \tag{34}$$

The exact solution to (32) and (33) for a horizontally uniform inertial wave in an *arbitrary* barotropic flow is

$$R = R_0, \tag{35}$$

$$\theta = \theta_0 - \frac{t}{2}\zeta(x, y, t), \tag{36}$$

$$\mathbf{k} = -\frac{t}{2}\nabla\zeta(x, y, t), \tag{37}$$

where R_0 and θ_0 are the initial uniform wave amplitude and phase. It is remarkable that the evolution of vorticity fully dictates the wave phase at all times. During the initial stages of evolution, ζ -refraction imprints the vorticity onto the phase, then phase and vorticity are subsequently advected by the same streamfunction. As a result, the spatial structure of the phase θ is slaved to the vorticity field for all time. Note that this solution crucially relies on the assumption that the inertial wave is initially horizontally uniform, $\mathbf{k}_0 = \nabla\theta_0 = \nabla R_0 = 0$.

We emphasize that this solution retains all processes in (30) except dispersion (and β -refraction, which is weak). In particular, (30) includes ζ -refraction, straining, and \mathbf{k} -advection and holds for an arbitrary barotropic flow, i.e., the flow is neither assumed steady nor spatially uniform. Moreover, the solution gives the evolution of \mathbf{k} at a fixed point in space, *not* following the wave packet. At all points in space and time, the wavevector \mathbf{k} is determined by the local instantaneous vorticity gradient. In a steady flow such as the dipole, \mathbf{k} grows linearly in time, consistent with the behavior in the jet center (Fig. 5) as well as in the confluent and diffluent regions (Fig. 8).

c. Validation

1) STEADY FLOW

Dispersive and nondispersive YBJ solutions for sea surface wave phase θ look qualitatively similar in the dipole case

(Fig. 9). The wave phase grows proportionally to the local $\zeta(x, y)$, such that vortex-shape annuli form. In accordance to (36), the phase of the nondispersive solution (middle panels, Fig. 9) is perfectly antisymmetric between the cyclonic and anticyclonic cores. Over time, this antisymmetry is broken in the dispersive solution (top panels, Fig. 9) by terms such as $-\hbar|\mathbf{k}|^2$ in (29), which is negative everywhere.

No wave energy propagation occurs without dispersion. The weakly dispersive solution does not predict what happens below the surface layer, where wave energy remains confined. That said, the wave phase solution at a depth of 200 m (bottom panels, Fig. 9) exhibits some similarities with the depth-independent nondispersive solution (middle panels, Fig. 9) in the anticyclone. In particular, phase contours largely align with streamlines, indicating weak Doppler shifts. Outside the anticyclone, there is almost no wave energy and the wave phase is not meaningful.

2) UNSTEADY FLOW

As a more challenging test of the weakly dispersive solution, the YBJ equation is integrated with the usual wave initial condition, but coupled with the NISKINE flow field (Fig. 1a). Contrary to the dipole flow, which is a steady solution of (34), the NISKINE flow is unsteady. This is clear from the rapid evolution of the vorticity contours in Fig. 10. Within a few inertial periods, isolines of vorticity are squeezed into filaments as enstrophy cascades forward and the flow becomes rapidly unrecognizable.

Overlaid on these vorticity contours are color maps of the sea surface wave phase θ . Vorticity contours enclose regions of relatively uniform wave phase, consistent with phase being slaved to vorticity. The dispersive (two top rows, Fig. 10) and nondispersive (bottom row, Fig. 10) solutions look qualitatively similar, although they begin to diverge significantly after 10 and 15 inertial periods.

d. Interpretation

1) STEADY FLOW

We finally return to one of the central question of this paper: why is straining ineffective in the dipole flow? The key is that both straining and \mathbf{k} -advection originate from the gradient of the Doppler shift (or phase advection):

$$\underbrace{\nabla J(\psi, \theta)}_{\text{Doppler shift}} = \underbrace{J(\psi, \mathbf{k})}_{\mathbf{k}\text{-advection}} + \underbrace{J(\nabla\psi, \theta)}_{\text{straining}}. \tag{38}$$

In a barotropic steady flow such as the dipole, contours of vorticity align with streamlines: $J(\psi, \zeta) = 0$ in (34) if $\partial_t \zeta = 0$. In the weakly dispersive limit, wave phase is slaved to vorticity (36) such that wave phase contours also align with streamlines (Fig. 9). Thus, \mathbf{k} is perpendicular to \mathbf{U} and the Doppler shift remains zero at all times:

$$J(\psi, \theta) = -\frac{1}{2}tJ(\psi, \zeta) = 0. \tag{39}$$

Consequently, \mathbf{k} -advection must cancel straining everywhere and at all times to satisfy (38) and (39):

$$\mathbf{k}\text{-advection} = -\text{straining}. \tag{40}$$

This is true provided that (i) the barotropic flow is steady and (ii) the initial phase of the wave is uniform. Condition (ii) is the usual assumption that the near-inertial wave is quickly generated by atmospheric forcing with large horizontal scales.

We can finally answer the question posed above: straining and \mathbf{k} -advection are both ineffective in the dipole because they cancel each other. The jet region of the dipole is dominated by weakly dispersive modes which have not yet escaped to the anticyclonic core. In accordance to (30), the Eulerian wavevector increases linearly with the local vorticity gradient,

$$\partial_t \mathbf{k} = -\frac{1}{2} \nabla \zeta(x, y), \tag{41}$$

consistent with Figs. 5 and 8. Only refraction modifies the wavevector.

Since the Doppler shift vanishes everywhere for steady flows in the weakly dispersive limit (38), the *intrinsic* wave frequency ω_i (16) is conserved along ray trajectories. Following section 4c, wave bands can be backtracked not only near the jet center, but anywhere.

2) UNSTEADY FLOW

In unsteady flows, the wavevector is also only determined by the local instantaneous vorticity gradient, (37). This seems to suggest that only refraction is acting. But this is not the case: straining also shapes the wavevector. Unlike the steady case, \mathbf{k} and \mathbf{U} are no longer perpendicular so Doppler shift is *not* zero in an unsteady flow:

$$J(\psi, \theta) = -\frac{t}{2} J(\psi, \zeta) = \frac{t}{2} \partial_t \zeta \neq 0. \tag{42}$$

The gradient of $J(\psi, \theta)$ still results in both \mathbf{k} -advection and straining via (38), but these processes no longer perfectly cancel:

$$\mathbf{k}\text{-advection} \neq -\text{straining}. \tag{43}$$

In unsteady flows, the rate of change of the wavevector is the sum of the local instantaneous vorticity gradient (pure refraction) plus a term due to the time dependence of vorticity, which encapsulates the noncanceling effects of straining and \mathbf{k} -advection:

$$\mathbf{k}_t = \underbrace{-\frac{1}{2} \nabla \zeta(x, y, t)}_{\text{refraction}} - \underbrace{\frac{t}{2} \partial_t \nabla \zeta(x, y, t)}_{\text{straining}}. \tag{44}$$

If the flow is steady, only refraction is effective and one recovers (41).

7. Energetics

To quantify the roles of refraction and straining in eddy-wave energy transfers, we introduce the volume-averaged refraction- (Γ_r) and advection-induced (Γ_a) production of wave potential energy (Rocha et al. 2018),

$$\Gamma_r \stackrel{\text{def}}{=} - \left\langle \frac{1}{2f} \nabla \zeta \cdot \mathbf{F} \right\rangle, \tag{45}$$

$$\Gamma_a \stackrel{\text{def}}{=} -\frac{1}{4N^2} \left\langle (A_{xz}^* \ A_{yz}^*) \begin{pmatrix} S_n & S_s \\ S_s & -S_n \end{pmatrix} \begin{pmatrix} A_{xz} \\ A_{yz} \end{pmatrix} \right\rangle, \tag{46}$$

where \mathbf{F} is the wave energy flux and A is defined in (5). Refraction produces wave potential energy ($\Gamma_r > 0$) when the wave energy flux goes against vorticity gradients, i.e., as wave energy propagates toward more anticyclonic regions. Straining produces wave potential energy ($\Gamma_a > 0$) when wave gradients are enhanced via geostrophic straining.

Figure 11a shows wave potential energy production for the dipole flow, with (solid lines) and without (dashed lines) dispersion. As predicted, the nondispersive dipole has exactly zero contribution from straining (green dashed line is zero). With dispersion, refraction (solid blue) dominates the early time creation of gradients as wave energy accumulates in the anticyclonic region. Straining (solid green) does kick in after a few inertial periods, but its magnitude remains relatively weak, compared with expectations from passive-scalar picture of straining. This is consistent with Fig. 9, in which wave phase lines remain nearly parallel to streamlines, such that $J(\psi, \theta) \approx 0$ and straining is largely cancelled by \mathbf{k} -advection.

Straining is more potent in the NISKINe flow (Fig. 11b) than in the dipole (Fig. 11a). This is because letting the flow evolve allows the generation of stronger flow gradients via the forward enstrophy cascade. Note that in contrast to the dipole, straining is not eliminated by removing dispersion (green dashed). Quite the contrary: straining is much stronger in the nondispersive than in the dispersive case for the NISKINe flow. In this case, waves cannot disperse and wave escape is impossible. Dissipation is correspondingly larger as waves are strained into oblivion.

8. Discussion

In this paper we examined the evolution of large-scale near-inertial waves in steady and unsteady barotropic flows, with an eye on how refraction and straining shape the wavevector. We now assemble the main findings of the previous sections and discuss their implications and limitations.

a. Wave bands along the dipole jet

Nearly monochromatic wave bands appear along the dipole jet as wave energy propagates downward and toward the anticyclonic drainpipe (Fig. 2). With the knowledge of stratification and vorticity gradient alone, one can predict the bands' horizontal (9) and vertical (12) wavenumbers and their slope (13). Although these results follow from analysis at the jet center, their validity extends along the axis of the jet. Conservation of the intrinsic frequency (16) allows one to backtrack the surface origin of wave bands observed at depth in the jet vicinity (section 4c). Finally, if the distribution of vertical wave modes is known, the radiation of wave energy out of the surface layer can be estimated (section 4d).

b. Straining is ineffective in steady barotropic flows

The weakly dispersive limit helps explain why wind-generated inertial waves do not experience a strain-induced exponential growth of $|\mathbf{k}|$ in barotropic steady flows. If the primordial wave has a horizontal scale larger than the eddies, ζ -refraction is the

only process acting initially. Vorticity imprints its scales onto wave phase, and both fields are subsequently advected by the same streamfunction. In barotropic steady flows, vorticity advection, and thus phase advection is zero everywhere (39). This means that the Doppler shift vanishes everywhere (39). As a result, $\mathbf{k} = -\nabla\zeta(x, y)t/2$ (Figs. 5 and 8). Note that this is true only of the weak-dispersion limit. When dispersion is included, straining operates, albeit more weakly than anticipated from the passive-scalar analogy (Fig. 11).

c. Straining is effective in unsteady barotropic flows

In the limit of weak dispersion, the wavevector grows proportionally to the local instantaneous vorticity gradient (37). This does *not* imply that the wavevector is only modified by refraction. Unsteady vorticity gradients are associated with straining (44). In the NISKINe flow, straining is actually more effective than refraction in producing wave gradients after a few inertial periods (Fig. 11).

d. Forward cascade of wave phase

Unsteady quasigeostrophic flows, by analogy with two-dimensional flows, promote a forward cascade of potential vorticity variance (Kraichnan 1967; Charney 1971). For barotropic flows, this implies a relentless enhancement of vorticity gradients via squeezing and stretching of filaments until statistical stationarity is attained (Fig. 10). In the weakly dispersive limit, the wave phase is slaved to vorticity (36). One therefore also expects a forward cascade of wave phase variance that is even faster than that of vorticity variance because of the additional t factor in (36). In other words, the wave phase rapidly becomes incoherent as a consequence of quasigeostrophic turbulence (Fig. 10).

As wave phase gradients ($\nabla\theta = \mathbf{k}$) are enhanced by this forward cascade, B_u increases and strengthens dispersive effects. Asselin and Young (2019) show that dispersion eventually arrests the forward cascade. This is consistent with the right panel of Fig. 11, which shows shear production by straining (green) and loss via dissipation (black) in the unsteady NISKINe flow. The dispersive solution (solid) suffers less straining and dissipation than the nondispersive solution (dashed) since wave escape upsets wave capture (Rocha et al. 2018).

e. Predictability of the wave phase in a barotropic flow

The weakly dispersive solution (36) promises strong predictive powers on the sea surface wave phase for both steady and unsteady barotropic flows. According to this solution, one can deduce the wave phase anywhere and anytime from the local instantaneous flow vorticity and time elapsed since the wave inception. The horizontal wavevector or wave frequency can similarly be predicted given the local instantaneous vorticity gradient or tendency. It is remarkable that wave dynamics do not explicitly depend on the *history* of the evolution of the barotropic flow—whatever happened between the wave inception and the time of measurement—but only on its *instantaneous* state. The wave phase also depends only on *spatially local* measurements of vorticity. The spatiotemporal locality of

the weakly dispersive solution makes it powerful for interpreting spatially and temporally sparse observational data.

With great predictive powers come great limitations. The weakly dispersive solution crucially depends on three restrictive assumptions: (i) the flow must be barotropic, (ii) the primordial horizontal scale of the wave must be much larger than eddies, and (iii) the waves must be weakly dispersive. This last assumption limits the validity of the weakly dispersive solution to early times following the wave inception, i.e., before a significant fraction of the wave energy is radiated away by the dispersive modes. Finally, the model’s predictive power is confined to the surface layer and does not extend to near-inertial waves propagating in the pycnocline because these waves are by definition dispersive.

The weakly dispersive solution is useful despite its limitations. Thomas et al. (2020) use the weakly dispersive solution (37) to explain the wavevector evolution observed in the unsteady NISKINe flow. In two distinct regions of the flow, time series of the wavenumber follow the observed local instantaneous vorticity gradient for several inertial periods. This is a strong test of the weakly dispersive solution, where $\nabla\zeta$ varies both in space and time.

Acknowledgments. We thank the NISKINe investigators for their valiant investments to obtain the measurements that motivated this study and constrained our initial conditions. We also thank Eric Kunze and an anonymous reviewer for their constructive comments on the manuscript. This work was supported by the National Science Foundation Award OCE-1657041 (O.A. and W.R.Y.) and by the Office of Naval Research Awards N00014-18-1-2780 (L.R.), N00014-18-1-2798 (L.N.T.), and N00014-18-1-2803 (O.A. and W.R.Y.). We are grateful for computer resources provided by the Extreme Science and Engineering Discovery Environment (XSEDE), which is supported by National Science Foundation Grant ACI-1548562.

APPENDIX A

Jet Region Solution

We seek a solution of the linear YBJ equation in the vicinity of the jet region, $\kappa x \ll 1$, and along the line joining the vortex cores ($y = 0$). Assuming constant f and N , YBJ (7) melts down to

$$A_{zzt} + \frac{i}{2}\zeta A_{zz} + i\frac{N^2}{2f}A_{xx} = 0. \tag{A1}$$

Following MLS, we seek for solutions of the form $A(x, z, t) = B(x, z, t) \exp(-i\zeta t/2)$. Substituting this ansatz into (A1) yields

$$B_{zzt} + \frac{N^2\zeta_x}{2f}tB_x = i\frac{N^2\zeta_x^2}{8f}t^2B - \frac{N^2\zeta_{xx}}{4f}tB - i\frac{N^2}{2f}B_{xx}. \tag{A2}$$

It is useful to nondimensionalize (A2) with

$$X = x\kappa, \quad Z = \frac{z}{\sigma}, \quad T = \frac{t}{\tau}, \quad \tau = \left(\frac{f}{N^2\gamma^2\sigma^2}\right)^{1/3}. \tag{A3}$$

Then, (A2) becomes

$$B_{ZZT} - \frac{1}{2}\eta\Gamma \cos XB B_X = \frac{i}{8}T^2 \cos^2 XB - \frac{1}{4}\eta T \sin XB - \frac{i}{2}\chi B_{XX}. \quad (A4)$$

Two dimensionless numbers emerge; using the typical dipole values we obtain

$$\eta = \frac{\kappa}{\gamma\tau} \approx 0.2, \quad \chi = \left(\frac{N^2\kappa^2\sigma^2}{f^2}\right)(\tau f) \approx 0.03, \quad (A5)$$

where $\tau \approx 2.5$ inertial periods. As such, the leading-order solution is dominated by

$$B_{zzt} \approx i \frac{N^2\zeta_x^2}{8f} t^2 B. \quad (A6)$$

To solve the above equation, we first take a Fourier transform in the vertical,

$$\hat{B}(m) = \int_{-\infty}^{\infty} B(z)e^{-imz} dz, \quad (A7)$$

where we assumed an infinite domain, i.e., the solution is largely concentrated near the surface so the bottom boundary can be neglected. B is extended evenly into positive z . The resulting ordinary differential equation has the solution

$$\hat{B} = \hat{B}_0 \exp\left(-i \frac{N^2\zeta_x^2 t^3}{24fm^2}\right). \quad (A8)$$

To recover the solution in terms of A , the inverse Fourier transform of (A8) is performed:

$$B(z, t) = \frac{1}{2\pi} \int_{-\infty}^{\infty} \hat{B}_0(m) e^{i\Phi} dm, \quad (A9)$$

where the phase Φ was introduced

$$\Phi \stackrel{\text{def}}{=} -\frac{N^2\zeta_x^2 t^3}{24fm^2} + mz. \quad (A10)$$

We can find an approximate solution to this integral using the method of stationary phase (e.g., Whitham 2011, and references therein). The idea is that the largest contributions to the integrand happen when the phase is stationary, i.e., when $\Phi_m = 0$, or

$$m^* = -\left(\frac{N^2\zeta_x^2}{12fz}\right)^{1/3} t. \quad (A11)$$

Expanding phase around m^* ,

$$\Phi(m) \approx \Phi(m^*) + (m - m^*) \underbrace{\Phi_m(m^*)}_{=0} + \frac{1}{2}(m - m^*)^2 \Phi_{mm}(m^*) + \dots \quad (A12)$$

Coming back to (A9), we pull all m -independent terms out of the integral:

$$B(z, t) \approx \frac{\hat{B}_0(m^*) \exp i\Phi(m^*)}{2\pi} \times \int_{-\infty}^{\infty} \exp\left[\frac{i}{2}(m - m^*)^2 \Phi_{mm}(m^*)\right] dm. \quad (A13)$$

Noting that $\Phi_{mm} = -N^2\zeta_x^2 t^3/4fm^4$ is always negative, the variable m is changed to $n = (m - m^*)\sqrt{|\Phi_{mm}(m^*)|/2}$:

$$B(z, t) \approx \frac{\hat{B}_0(m^*) \exp i\Phi(m^*)}{\pi\sqrt{2|\Phi_{mm}(m^*)|}} \int_{-\infty}^{\infty} \exp(-in^2) dn. \quad (A14)$$

These are Fresnel integrals and can be evaluated exactly:

$$\int_{-\infty}^{\infty} \exp(-in^2) dn = \sqrt{\pi} e^{-im/4}. \quad (A15)$$

Consequently,

$$B(z, t) \approx \frac{\hat{B}_0(m^*) \exp i[\Phi(m^*) - \pi/4]}{\sqrt{2\pi|\Phi_{mm}(m^*)|}}. \quad (A16)$$

To obtain an expression for $\hat{B}_0(m^*)$ we Fourier transform the wave initial condition (4):

$$\begin{aligned} \widehat{L}A_0 &= u_0 \int_{-\infty}^{\infty} \exp[-(z/\sigma)^2 - imz] dz \\ &= u_0\sigma\sqrt{\pi} \exp(-m^2\sigma^2/4). \end{aligned} \quad (A17)$$

Then, we can evaluate $\hat{B}_0(m^*)$, which is $-(N/fm)^2 \widehat{L}A_0$ evaluated at m^* . Plugging back all expressions into the solution (A16) and bringing back the x -dependent part of the solution:

$$A(x, z, t) \approx \frac{\sqrt{2}u_0 N\sigma}{\zeta_x(f t)^{3/2}} \exp\left[i\left(\Phi^* - \frac{\pi}{4} - \frac{\zeta}{2}t\right) - \frac{m^{*2}\sigma^2}{4}\right], \quad (A18)$$

where $\Phi^* \stackrel{\text{def}}{=} \Phi(m^*) = (3/2)m^*z$. Finally, applying the L operator on (A18) to get the solution in terms of the back-rotated wave velocity,

$$LA = F(x, z, t) \exp\left[i\left(\Phi^* - \frac{\pi}{4} - \frac{\zeta}{2}t\right) - \frac{m^{*2}\sigma^2}{4}\right], \quad (A19)$$

with

$$F(x, z, t) = -\frac{u_0\sigma}{\sqrt{6zm^{*3}}} [\Gamma_{zz} + (\Gamma_z)^2]. \quad (A20)$$

Above, Γ is the bracketed expression in (A19), whose derivatives are

$$\Gamma_z = im^* + \frac{1\sigma^2 m^{*2}}{6z}, \quad (A21)$$

$$\Gamma_{zz} = -i \frac{m^*}{3z} - \frac{5}{18} \left(\frac{\sigma m^*}{z}\right)^2. \quad (A22)$$

One can predict the wavenumbers characterizing the monochromatic leading-order solution by differentiating the phase of (A19):

$$k \stackrel{\text{def}}{=} \frac{\partial}{\partial x} \left(\Phi^* - \frac{\zeta}{2} t \right) = -\frac{1}{2} \zeta_x t + \frac{\zeta_{xx}}{\zeta_x} m^* z \approx -\frac{1}{2} \zeta_x t, \quad (\text{A23})$$

$$m \stackrel{\text{def}}{=} \frac{\partial}{\partial z} \left(\Phi^* - \frac{\zeta}{2} t \right) = m^* = \left(\frac{N^2 \zeta_x^2}{12f|z|} \right)^{1/3} t. \quad (\text{A24})$$

At the jet center, $\zeta_{xx} = 0$ and the heuristic predictions (9) and (12) are recovered, except that here ζ_x may be an arbitrary, albeit slowly varying function of x .

APPENDIX B

Estimating Wavenumbers

The back-rotated velocity is

$$\mathbf{L}\mathbf{A} = R e^{i\theta}, \quad (\text{B1})$$

where R and θ are both real. For any space or time variable α ,

$$\frac{\mathbf{L}\mathbf{A}_\alpha}{\mathbf{L}\mathbf{A}} = \frac{R_\alpha}{R} + i\theta_\alpha \Rightarrow \theta_\alpha = \Im \left(\frac{\mathbf{L}\mathbf{A}_\alpha}{\mathbf{L}\mathbf{A}} \right). \quad (\text{B2})$$

This rule permits the calculation of local Eulerian frequency and wavenumbers at every point in space and time which, in the WKB framework, are defined as

$$\omega \stackrel{\text{def}}{=} -\theta_t, \quad \mathbf{k} \stackrel{\text{def}}{=} \theta_x. \quad (\text{B3})$$

REFERENCES

- Alford, M. H., J. A. MacKinnon, H. L. Simmons, and J. D. Nash, 2016: Near-inertial internal gravity waves in the ocean. *Annu. Rev. Mar. Sci.*, **8**, 95–123, <https://doi.org/10.1146/annurev-marine-010814-015746>.
- Asselin, O., and W. R. Young, 2019: An improved model of near-inertial wave dynamics. *J. Fluid Mech.*, **876**, 428–448, <https://doi.org/10.1017/jfm.2019.557>.
- , and —, 2020: Penetration of wind-generated near-inertial waves into a turbulent ocean. *J. Phys. Oceanogr.*, **50**, 1699–1716, <https://doi.org/10.1175/JPO-D-19-0319.1>.
- , P. Bartello, and D. N. Straub, 2018: On Boussinesq dynamics near the tropopause. *J. Atmos. Sci.*, **75**, 571–585, <https://doi.org/10.1175/JAS-D-17-0097.1>.
- Asselin, R., 1972: Frequency filter for time integrations. *Mon. Wea. Rev.*, **100**, 487–490, [https://doi.org/10.1175/1520-0493\(1972\)100<0487:FFFTI>2.3.CO;2](https://doi.org/10.1175/1520-0493(1972)100<0487:FFFTI>2.3.CO;2).
- Balmforth, N. J., S. G. Llewellyn Smith, and W. R. Young, 1998: Enhanced dispersion of near-inertial waves in an idealized geostrophic flow. *J. Mar. Res.*, **56** (1), 1–40, <https://doi.org/10.1357/002224098321836091>.
- Bretherton, F. P., and C. J. R. Garrett, 1968: Wavetrains in inhomogeneous moving media. *Proc. Roy. Soc. London*, **A302**, 529–554, <https://doi.org/10.1098/RSPA.1968.0034>.
- Bühler, O., and M. E. McIntyre, 2005: Wave capture and wave-vortex duality. *J. Fluid Mech.*, **534**, 67–95, <https://doi.org/10.1017/S0022112005004374>.
- Charney, J. G., 1971: Geostrophic turbulence. *J. Atmos. Sci.*, **28**, 1087–1095, [https://doi.org/10.1175/1520-0469\(1971\)028<1087:GT>2.0.CO;2](https://doi.org/10.1175/1520-0469(1971)028<1087:GT>2.0.CO;2).
- Danioux, E., J. Vanneste, and O. Bühler, 2015: On the concentration of near-inertial waves in anticyclones. *J. Fluid Mech.*, **773**, R2, <https://doi.org/10.1017/JFM.2015.252>.
- D’Asaro, E. A., 1985: Upper ocean temperature structure, inertial currents, and Richardson numbers observed during strong meteorological forcing. *J. Phys. Oceanogr.*, **15**, 943–962, [https://doi.org/10.1175/1520-0485\(1985\)015<0943:UOTSIC>2.0.CO;2](https://doi.org/10.1175/1520-0485(1985)015<0943:UOTSIC>2.0.CO;2).
- , 1989: The decay of wind-forced mixed layer inertial oscillations due to the β effect. *J. Geophys. Res.*, **94**, 2045–2056, <https://doi.org/10.1029/JC094iC02p02045>.
- , C. C. Eriksen, M. D. Levine, C. A. Paulson, P. Niiler, and P. Van Meurs, 1995: Upper-ocean inertial currents forced by a strong storm. Part I: Data and comparisons with linear theory. *J. Phys. Oceanogr.*, **25**, 2909–2936, [https://doi.org/10.1175/1520-0485\(1995\)025<2909:UOICFB>2.0.CO;2](https://doi.org/10.1175/1520-0485(1995)025<2909:UOICFB>2.0.CO;2).
- Durrant, D. R., 2013: *Numerical Methods for Wave Equations in Geophysical Fluid Dynamics*. Text in Applied Mathematics, Vol. 32, Springer, 466 pp.
- Elipot, S., R. Lumpkin, and G. Prieto, 2010: Modification of inertial oscillations by the mesoscale eddy field. *J. Geophys. Res.*, **115**, C09010, <https://doi.org/10.1029/2009JC005679>.
- Geisler, J. E., 1970: Linear theory of the response of a two layer ocean to a moving hurricane. *Geophys. Astrophys. Fluid Dyn.*, **1**, 249–272, <https://doi.org/10.1080/03091927009365774>.
- Gill, A., 1984: On the behavior of internal waves in the wakes of storms. *J. Phys. Oceanogr.*, **14**, 1129–1151, [https://doi.org/10.1175/1520-0485\(1984\)014<1129:OTBOIW>2.0.CO;2](https://doi.org/10.1175/1520-0485(1984)014<1129:OTBOIW>2.0.CO;2).
- Jaimes, B., and L. K. Shay, 2010: Near-inertial wave wake of Hurricanes Katrina and Rita over mesoscale oceanic eddies. *J. Phys. Oceanogr.*, **40**, 1320–1337, <https://doi.org/10.1175/2010JPO4309.1>.
- Jones, W. L., 1969: Ray tracing for internal gravity waves. *J. Geophys. Res.*, **74**, 2028–2033, <https://doi.org/10.1029/JB074i008p02028>.
- Klein, P., S. L. Smith, and G. Lapeyre, 2004: Organization of near-inertial energy by an eddy field. *Quart. J. Roy. Meteor. Soc.*, **130**, 1153–1166, <https://doi.org/10.1256/QJ.02.231>.
- , B. L. Hua, G. Lapeyre, X. Capet, S. Le Gentil, and H. Sasaki, 2008: Upper ocean turbulence from high-resolution 3d simulations. *J. Phys. Oceanogr.*, **38**, 1748–1763, <https://doi.org/10.1175/2007JPO3773.1>.
- Kraichnan, R. H., 1967: Inertial ranges in two-dimensional turbulence. *Phys. Fluids*, **10**, 1417–1423, <https://doi.org/10.1063/1.1762301>.
- Kunze, E., 1985: Near-inertial wave propagation in geostrophic shear. *J. Phys. Oceanogr.*, **15**, 544–565, [https://doi.org/10.1175/1520-0485\(1985\)015<0544:NIWPIG>2.0.CO;2](https://doi.org/10.1175/1520-0485(1985)015<0544:NIWPIG>2.0.CO;2).
- , 1986: The mean and near-inertial velocity fields in a warm-core ring. *J. Phys. Oceanogr.*, **16**, 1444–1461, [https://doi.org/10.1175/1520-0485\(1986\)016<1444:TMANIV>2.0.CO;2](https://doi.org/10.1175/1520-0485(1986)016<1444:TMANIV>2.0.CO;2).
- , R. W. Schmitt, and J. M. Toole, 1995: The energy balance in a warm-core ring’s near-inertial critical layer. *J. Phys. Oceanogr.*, **25**, 942–957, [https://doi.org/10.1175/1520-0485\(1995\)025<0942:TEBIAW>2.0.CO;2](https://doi.org/10.1175/1520-0485(1995)025<0942:TEBIAW>2.0.CO;2).
- Lee, D.-K., and P. P. Niiler, 1998: The inertial chimney: The near-inertial energy drainage from the ocean surface to the deep layer. *J. Geophys. Res.*, **103**, 7579–7591, <https://doi.org/10.1029/97JC03200>.
- Lighthill, M., 1978: *Waves in Fluids*. Cambridge University Press, 504 pp.
- Moehlis, J., and S. G. Llewellyn Smith, 2001: Radiation of mixed layer near-inertial oscillations into the ocean interior. *J. Phys. Oceanogr.*, **31**, 1550–1560, [https://doi.org/10.1175/1520-0485\(2001\)031<1550:ROMLNI>2.0.CO;2](https://doi.org/10.1175/1520-0485(2001)031<1550:ROMLNI>2.0.CO;2).
- Nilsson, J., 1995: Energy flux from traveling hurricanes to the oceanic internal wave field. *J. Phys. Oceanogr.*, **25**, 558–573,

- [https://doi.org/10.1175/1520-0485\(1995\)025<0558:EFFTHT>2.0.CO;2](https://doi.org/10.1175/1520-0485(1995)025<0558:EFFTHT>2.0.CO;2)
- Pollard, R., 1980: Properties of near-surface inertial oscillations. *J. Phys. Oceanogr.*, **10**, 385–398, [https://doi.org/10.1175/1520-0485\(1980\)010<0385:PONSIO>2.0.CO;2](https://doi.org/10.1175/1520-0485(1980)010<0385:PONSIO>2.0.CO;2).
- Polzin, K. L., 2008: Mesoscale eddy–internal wave coupling. Part I: Symmetry, wave capture, and results from the mid-ocean dynamics experiment. *J. Phys. Oceanogr.*, **38**, 2556–2574, <https://doi.org/10.1175/2008JPO3666.1>.
- Price, J. F., 1983: Internal wave wake of a moving storm. Part I. Scales, energy budget and observations. *J. Phys. Oceanogr.*, **13**, 949–965, [https://doi.org/10.1175/1520-0485\(1983\)013<0949:IWWOAM>2.0.CO;2](https://doi.org/10.1175/1520-0485(1983)013<0949:IWWOAM>2.0.CO;2).
- Rocha, C. B., G. L. Wagner, and W. R. Young, 2018: Stimulated generation: Extraction of energy from balanced flow by near-inertial waves. *J. Fluid Mech.*, **847**, 417–451, <https://doi.org/10.1017/jfm.2018.308>.
- Thomas, L. N., L. Rainville, O. Asselin, W. R. Young, J. Girton, C. B. Whalen, L. Centurioni, and V. Hormann, 2020: Direct observations of near-inertial wave ζ -refraction in a dipole vortex. *Geophys. Res. Lett.*, <https://doi.org/10.1029/2020GL090375>, in press.
- Thomson, R. E., and W. S. Huggett, 1981: Wind-driven inertial oscillations of large spatial coherence. *Atmos.–Ocean*, **19**, 281–306, <https://doi.org/10.1080/07055900.1981.9649116>.
- Van Meurs, P., 1998: Interactions between near-inertial mixed layer currents and the mesoscale: The importance of spatial variabilities in the vorticity field. *J. Phys. Oceanogr.*, **28**, 1363–1388, [https://doi.org/10.1175/1520-0485\(1998\)028<1363:IBNIML>2.0.CO;2](https://doi.org/10.1175/1520-0485(1998)028<1363:IBNIML>2.0.CO;2).
- Weller, R. A., 1985: Near-surface velocity variability at inertial and subinertial frequencies in the vicinity of the California current. *J. Phys. Oceanogr.*, **15**, 372–385, [https://doi.org/10.1175/1520-0485\(1985\)015<0372:NSVVAI>2.0.CO;2](https://doi.org/10.1175/1520-0485(1985)015<0372:NSVVAI>2.0.CO;2).
- Whitham, G. B., 2011: *Linear and Nonlinear Waves*. Pure and Applied Mathematics Series, Vol. 42, John Wiley & Sons, 660 pp.
- Young, W. R., and M. Ben Jelloul, 1997: Propagation of near-inertial oscillations through a geostrophic flow. *J. Mar. Res.*, **55**, 735–766, <https://doi.org/10.1357/0022240973224283>.